Enhancing Glycerol Electrooxidation from Synergistic Interactions of Platinum and Transition Metal Carbides

Hansen Mou^{a1}, Qiaowan Chang^{a1}, Zhenhua Xie^b, Sooyeon Hwang^c, Shyam Kattel^d, and Jingguang G. Chen^{a,b}*

^aDepartment of Chemical Engineering, Columbia University, New York, NY 10027, USA

^bChemistry Division, Brookhaven National Laboratory, Upton, New York 11973, USA

^cCenter for Functional Nanomaterials, Brookhaven National Laboratory, Upton, New York 11973, USA

^dDepartment of Physics, Florida A&M University, Tallahassee, FL 32307

¹These authors contributed equally.

^{*} Corresponding Author: jgchen@columbia.edu

Abstract

To effectively utilize glycerol as a fuel for electrochemical fuel cells, it is necessary to optimize catalysts for effective C-C bond cleavage and complete oxidation of reaction intermediates to achieve maximum efficiency. The current work showed that the synergistic interactions of platinum (Pt) with transition metal carbide (TMC) substrates, such as tungsten carbide (WC) and tantalum carbide (TaC), fulfilled these criteria. The TMC-supported Pt catalysts showed higher activity and selectivity for complete glycerol oxidation than commercial 10 wt% Pt/C. *In-situ* FTIR analysis revealed that 5 wt% Pt/WC was the most effective catalyst among those tested for complete glycerol oxidation at 0.9 V vs RHE. *In-situ* X-ray absorption fine structure characterization and density functional theory calculations provided additional insight into the synergistic interactions for glycerol oxidation over Pt/TMC catalysts.

Key words: Glycerol electrooxidation; Pt-modified transition metal carbides; *in-situ* Fourier transform infrared spectroscopy; *in-situ* X-ray absorption.

1. Introduction

Decades of growth in biodiesel production has led to potential market saturation of glycerol, which is the main byproduct from biodiesel, as about 1 kg of glycerol is produced for every 10 kg of biodiesel [1,2]. While glycerol possesses remarkable versatility in applications ranging from food and pharmaceuticals to polymers and cosmetics, refining the crude glycerol from biodiesel production is uneconomical for small and medium sized biodiesel producers [1,3]. Thus, glycerol valorization has drawn much interest [4–6], including electrochemical conversion of glycerol to produce both energy and value-added products, as shown in Figure 1. Among these electrochemical reactions, only the complete oxidation of glycerol enables the complete utilization of energy in the molecule [7]. This would enable crude glycerol to serve as a cost-effective fuel similar to direct methanol and ethanol fuel cells.

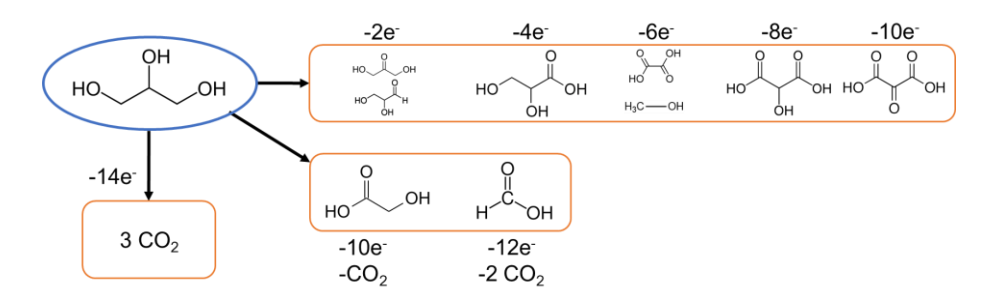


Figure 1. Possible products for the electrochemical oxidation of glycerol.

Alcohol and glycerol oxidation in alkaline conditions has been found to exhibit improved performance due to its faster kinetics, with the first alcohol deprotonation step being base-catalyzed [8,9]. To generate the most electrons from glycerol as an anodic fuel, catalysts should be optimized for the complete scission of all C-C bonds, as well as for completely oxidizing any intermediates before desorption. Previous studies with methanol and ethanol have demonstrated that Pt-modified TMCs can fulfill both criteria [10–12].

Pt-based catalysts have long been the material of choice for alcohol and polyol oxidation [13–18]. However, aside from its scarcity, the utilization of Pt has also been hindered by sluggish kinetics primarily due to the high binding energy of carbon monoxide (CO), effectively poisoning the catalyst. Supporting Pt

on TMCs has been shown to reduce the CO binding strength, as in the case reported for Pt supported on tungsten carbide (Pt/WC) and tantalum carbide (Pt/TaC) [10,11,19]. TMCs have attracted attention as a versatile class of materials that can exhibit catalytic properties similar to those of Pt-group metals (PGMs) [20]. Incorporating carbon atoms in the crystal lattice of the parent transition metal causes the bond length between metal atoms to lengthen, thereby changing the d-band electron density of the metal at the Fermi level [21]. The synergistic interactions between Pt and TMCs have also been shown to enhance the overall electrocatalyst activity by reducing the onset potential and increasing current density. This enhancement is the result of adsorbed hydroxyl and oxygen species formation on TMCs, which promote the electrooxidation of adsorbed carbonate and CO species and accelerate their removal from the surface through the "bifunctional mechanism" [15,22–24]. Furthermore, both Pt/TaC and Pt/WC have been shown to preferentially catalyze the scission of the C-C bond for ethanol oxidation [10,11].

This work investigated the extent to which these key properties affected the oxidation of more complex polyols such as glycerol. To that end, TaC and WC were synthesized and modified with varying quantities of Pt to investigate the synergistic effect of supporting Pt on TaC and WC supports for electrochemical glycerol oxidation. The electrocatalytic activities were measured via cyclic voltammetry, while the reaction products and intermediates were further examined with FTIR spectroscopy. The catalysts were characterized using X-ray absorption fine structure (XAFS) under *in-situ* electrocatalytic conditions. DFT calculations were also performed to identify the effect of Pt and TMC interactions on the binding energies of glycerol and CO.

2. Experimental Methods

2.1 Catalyst Synthesis and Characterization

Procedures for synthesizing powder TaC and WC, and the subsequent modification with 2.5 wt%, 5 wt%, and 10 wt% Pt via the NaOH-assisted ethylene glycol reduction method were adapted from Wang et al. [25]. Powder TaC was prepared by mixing TaCl₅ with ethanol and grinding with MCM-41 until the ethanol had evaporated. The dried powder was carburized in a tubular quartz reactor before it was then

cooled and passivated. The resulting powder was etched in 2 M NaOH for 2 hours to remove the MCM-41 before rinsing and drying. Powder WC was prepared similarly but using ammonium metatungstate hydrate (NH₄)₆H₂W₁₂O₄₀•xH₂O) as the precursor. The procedure for modifying the TaC and WC with Pt was adjusted so that the appropriate amount of K₂PtCl₄ was dissolved in 1 mL of deionized water before application. The Pt loadings were verified by dissolving in aqua regia overnight before diluting and analyzing with ICP-OES. Commercial 10 wt% Pt on Vulcan XC-72 catalyst (E-TEK, De Nora North America Inc.) was used as the benchmark for comparison.

Powder catalysts were characterized using X-ray photoelectron spectroscopy (XPS) in an ultrahigh vacuum (UHV) chamber at a base pressure $< 7 \times 10^{-9}$ Torr using an Al K α X-ray source. The energy was calibrated using adventitious carbon at 284.5 eV. Symmetric XRD scans were performed using a Cu K α X-ray source directed on a spinning stage. The results were compared against reference patterns #243678, #159875, and #246149 from the Inorganic Crystal Structure Database.

The transmission electron microscopy (TEM) characterization of catalyst particles was performed at Center for Functional Nanomaterials, Brookhaven National Laboratory. High-angle annular dark-field scanning TEM (HAADF-STEM) images and energy dispersive X-ray spectroscopy (EDS) elemental maps were obtained with Themo-Fisher Talos F200X at an accelerating voltage of 200 kV.

2.2 Electrode Preparation and Characterization

The powder catalyst was used to prepare electrode ink by mixing 6 mg of catalyst, 0.264 mL deionized water, 0.183 mL isopropanol, and 0.058 mL 5% Nafion-117. The mixture was sonicated for 1 hour. Then, 42 μ L of ink was drop-casted onto 1 cm² of Toray carbon paper and left to dry at room temperature overnight. The resulting electrodes had a catalyst loading of about 0.5 mg/cm².

The electrochemically active surface area (ECSA) of the electrodes was measured via copper (Cu) stripping to normalize electrochemical data and account for surface roughness. The procedure was adapted from Wang et al. [26]. Cu stripping was performed in a 3-electrode cell, where carbon paper electrodes were first cycled in 0.5 M H₂SO₄ between -0.9 V and 0 V vs Ag/AgCl for 25 cycles at 50 mV/s. Then, in

the same electrolyte, the electrodes were held at 0.25~V vs RHE for 60 seconds before sweeping to 0.8~V vs RHE at 50~mV/s to establish a baseline. Next, the electrodes were transferred to another 3-electrode cell with $0.5~M~H_2SO_4$ and $2~mM~CuSO_4$, where the electrodes were held at 0.25~V vs RHE for 300 seconds before sweeping up to 0.8~V vs RHE at 50~mV/s. ECSA was calculated from the area between the resulting plot and the baseline, corresponding to the charge necessary for stripping monolayer adsorbed Cu from the surface, and dividing the result by the charge density for Cu, $420~\mu C/cm^2$. All potentials written hereafter are referenced against RHE.

2.3 Electrochemical Evaluation of Glycerol Oxidation

Catalysts were tested in 3-electrode cells, with the catalyst electrode as the working electrode, a graphite rod as the counter electrode, and a saturated calomel electrode as the reference electrode. The electrolytes used were 0.1 M KOH with and without 1 M glycerol. After the cells were purged with argon for 10 minutes, cyclic voltammetry (CV) between 0.1V and 1.4 V were performed for 4 cycles at 50 mV/s in only 0.1 M KOH to clean the electrode. Next, CV for 20 cycles in 0.1 M KOH with 1 M glycerol between 0.1V to 1.4V at 50 mV/s was performed. Electrochemical Impedance Spectroscopy (EIS) was then performed in 0.1 M KOH with 1 M glycerol to measure the ohmic resistance, with which the appropriate iR compensation was corrected for in the subsequent chronoamperometry (CA) experiment. The CA for each catalyst was performed at 0.6 V for 1 hour in the argon-purged 3-electrode cell containing 0.1 M KOH with 1 M glycerol to compare catalyst stability and activity over time.

2.4 In-situ FTIR Measurements

In-situ FTIR spectroscopy (Nicolet IS50 spectrometer equipped with a mercuric cadmium telluride detector) measurements were performed in a home-made 3-electrode cell setup similar to that of the CV scans. The spectra were first obtained in 0.1 M KOH with 1 M glycerol solution between 0.1V to 1.4V with the scan rate of 2 mV/s. The acquired spectra were processed by subtracting the first reference spectrum as the background.

2.5 In-situ X-ray Absorption Fine Structure (XAFS) Measurements

The XAFS results of the Pt L₃ or L₂ edge were measured *in-situ* at beamline 7-BM (QAS, 10¹² ph/s⁻ at 10 keV) of the National Synchrotron Light Source II (NSLS-II) at Brookhaven National Laboratory. The *in-situ* experiments were conducted using a home-made acryl H-type cell with two Kapton windows for beam penetration [27]. The working electrode and electrolyte were the same as those used in the electrochemical testing of glycerol oxidation. For each measurement, the electrode was cleaned in 0.1 M KOH via CV between 0.1 and 1.4 V for 4 cycles at 50 mV/s. Afterwards, the electrolyte was immediately replaced with 0.1 M KOH and 1 M glycerol solution, followed by additional 20 cycles of CV between 0.1 and 1.4 V at 50 mV/s. The CA for each catalyst was subsequently carried out at the open circuit (OC, 0.0), 0.3, 0.6, 0.9, and 1.1 V, at which potential the reaction was retained for 20 min to reach the steady state. Both the transmission and fluorescence signals were simultaneously collected at a rate of 2 scans/min.

The X-ray absorption near edge structure (XANES) and extended X-ray absorption fine structure (EXAFS) spectra were measured at the Pt L₃ edge (11564 eV) for the Pt/C and Pt/TaC samples. Because the L₂ (11136 eV) and L₁ (11682 eV) edges of Ta were close to the Pt L₃ edge, the pre-edge region of the Pt L₃ edge XANES was slightly distorted by the EXAFS oscillation of the Ta L₂ edge, while the EXAFS region (at ca. 100 eV above the edge) was strongly interfered by the Ta L₁ edge EXAFS feature. As for Pt/WC, the Pt L₂ edge was collected instead due to the severe interference of Pt L₃ edge (11564 eV) with W L₂ edge (11544 eV). The energy shift was calibrated by a Pt foil, which was also used for XANES comparison. Data processing was preformed using the IFEFFIT package [28,29].

2.6 DFT Calculations

A plane wave Vienna Ab-Initio Simulation Package (VASP) code [30,31] was used to perform spin polarized density functional theory (DFT) calculations [32,33]. The core electrons were described using the projector augmented wave (PAW) potentials [34] within the generalized gradient approximation [35] using

PW91 functionals [36]. A kinetic energy cutoff of 400 eV and $3 \times 3 \times 1$ k-point mesh were used in all structure optimization calculations.

The Pt(111) surface was modeled using a 4 layer 3 × 3 surface slab. One monolayer (ML) of Pt was optimized on Ta terminated TaC(111) and W terminated WC(001) surfaces to model Pt/TaC and Pt/WC catalysts, respectively. A vacuum layer of ~18 Å thick was added to the slab cell along the direction perpendicular to the surface to minimize the artificial interactions between the surface and its periodic images. Atoms in the bottom two layers were fixed while all other atoms were allowed to relax during geometry optimization until the Hellmann–Feynman force on each ion was smaller than 0.02 eV/Å.

The binding energy (BE) of adsorbate was calculated as:

BE(adsorbate) = E(slab + adsorbate) - E(slab) - E(adsorbate)

where E(slab + adsorbate), E(slab), and E(adsorbate) are the total energies of the slab with adsorbate, clean slab and adsorbate species in the gas phase, respectively.

3. Results and Discussion

3.1 Catalyst Characterization

Results from the symmetric XRD for the Pt-modified TMC powders suggested TaC and WC retained the crystal structure of the bulk materials. The diffractograms for the Pt-modified samples showed broad peaks for the Pt, some of which were indistinguishable from the baseline (Figure S1), suggesting small particle sizes and good Pt dispersion. These results are similar to those reported by Wang et al. [25], where XRD showed broad peaks for the palladium (Pd) modifier, and STEM-EDS revealed that this method had indeed deposited finely dispersed Pd nanoparticles on the surface of TMC powders. To confirm that the broad XRD Pt peaks were a result of high dispersion, ICP-OES was used to verify the presence of Pt in the Pt/TMC samples. Using the commercial 10 wt% Pt/C and diluted Pt standards for ICP-OES as references, the synthesized catalysts were found to have Pt loadings within 25% of the nominal loadings (Table S1).

The Pt particles sizes and Pt/TMC elemental compositions were analyzed using HAADF-STEM imaging and STEM-EDS elemental mapping (Figure 2). The commercial 10 wt% Pt/C showed an average particle size calculated to be 2.1 nm (Figure 2a). The Pt was less distinguishable on the TMC-supported catalysts due to the limited Z-contrast between the Pt, Ta and W. Nonetheless, the average particle size for 10 wt% Pt/TaC was estimated to be 3.1 nm, though with some outliers observed on the order of 10 nm (Figure 2b). Similarly, the average particle size for 10 wt% Pt/WC was observed to be 3.6 nm, with some outliers observed on the order of 15 nm (Figure 2c).

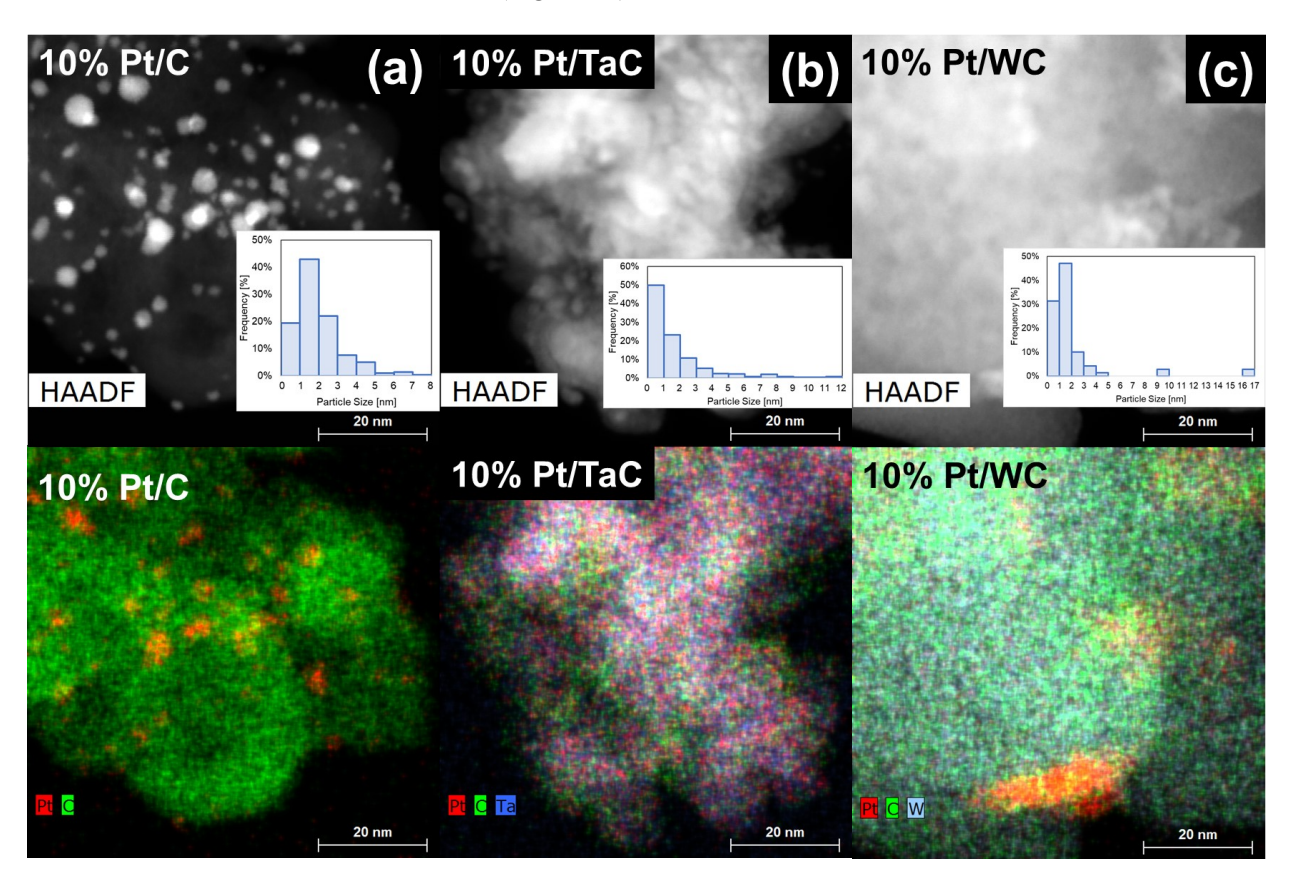


Figure 2. HAADF-STEM images with corresponding particle size histograms and STEM-EDS elemental mapping for (a) 10 wt% Pt/C, (b) 10 wt% Pt/TaC, and (c) 10 wt% Pt/WC.

The Pt/TMC catalysts were analyzed before and after the electrochemical experiments for their oxidation states and elemental compositions using XPS. The XPS of Pt 4f features indicated the Pt to be in its metallic state in both Pt/TaC and Pt/WC, as suggested by the metallic Pt peak at ~71 eV (Figure S3). For Pt/TaC, the Ta 4f region showed a significant decrease of TaC after use, likely attributed to the high

oxidative potentials relative to the reported TaC stability regime in alkaline conditions [37]. However, the Pt/Ta peak area ratios remained relatively unchanged, with the fresh 10 wt% Pt/TaC electrode at 1.87 and the spent electrode at 1.84, indicating that Pt was stable on the TaC support during electrochemical testing (Table S2). For Pt/WC, though the Pt remained metallic, the W 4f region revealed peaks for W⁶⁺ (WO₃) and W⁴⁺ (WO₂) for the fresh 10 wt% Pt/WC electrode (Figure S4). The spent electrode then revealed a decrease in the W⁶⁺ peaks while the other peaks remained relatively unchanged. These results could be explained by the dissolution of WO₃ in the aqueous electrolyte, which had been reported WO₃ at pH greater than 3 [38]. As a result of the decrease in WO₃, the spent 10 wt% Pt/WC electrode showed a larger Pt/W peak area ratio of 0.345, as compared to the fresh electrode at 0.185 (Table S2).

3.2 Electrochemical Measurements

Among all the catalysts tested, the commercial Pt/C catalyst showed the highest activity by geometric surface area due to better Pt dispersion. As compared in Table 1, the commercial 10 wt% Pt/C showed the largest ECSA, with 67.3 cm²/mg_{cat}, which fell within the range of reported values in the literature [39–42]. The 10 wt% Pt/TaC and 10 wt% Pt/WC showed 21.0 cm²/mg_{cat} and 14.3 cm²/mg_{cat}, respectively. The ECSA values decreased for catalysts with 5 wt% and 2.5 wt% Pt catalysts, although they did not show a linear correlation with the metal loading. This suggested that increasing the Pt loading might have resulted in increased particle agglomeration, thereby reducing the available surface area relative to the mass of Pt.

Table 1. ECSA of catalysts in this study measured by Cu stripping.

Catalyst	ECSA [cm ² /mg _{cat}]
10 wt% Pt/C	67.3
10 wt% Pt/TaC	18.7
5 wt% Pt/TaC	14.8
2.5 wt% Pt/TaC	7.6
10 wt% Pt/WC	14.3
5 wt% Pt/WC	12.9

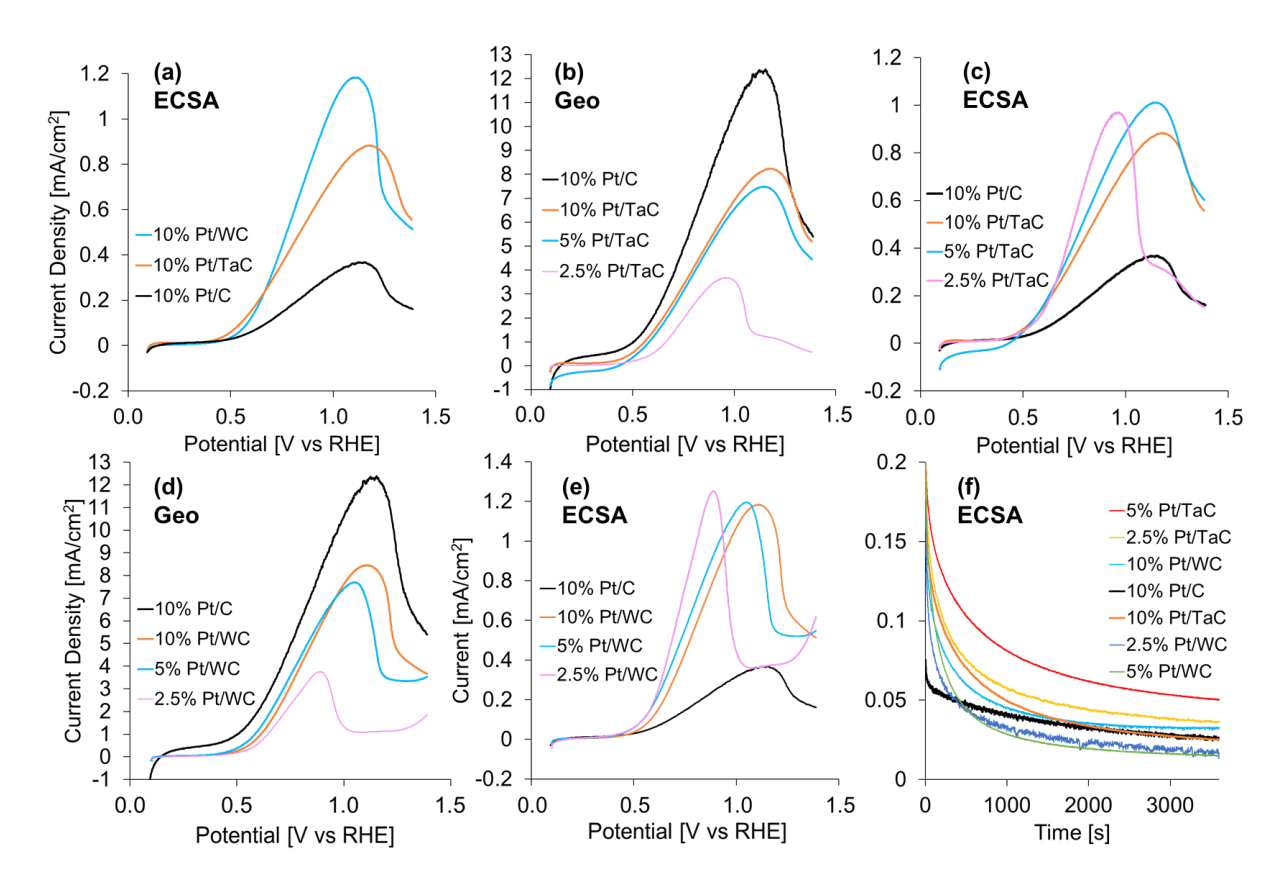


Figure 3. Positive sweeps for the 20th CVs for Pt/TaC normalized by (a) geometric surface area, (b) ECSA; (c) 10 wt% Pt/TMC normalized by ECSA; Pt/WC normalized by (d) geometric surface area, (e) ECSA; 1 hour CA data at 0.6 V vs RHE, normalized by (f) ECSA.

Once accounting for ECSA, it became evident that the high activity from Pt/C was the result of higher surface area, and that using TMCs as supports enhanced the overall catalytic activity per unit of available surface area (Figure 3a). Varying the Pt mass loading on TaC from 10 wt% to 5 wt% yielded little change in activity from the CVs on the basis of geometric surface area, while 2.5 wt% showed about half of the peak activity of 10 wt% Pt/TaC (Figure 3b). Normalizing the data by ECSA showed that the three Pt/TaC catalysts showed similar activity, suggesting that the activity was related to the number of Pt sites.

The results for Pt/WC revealed a similar trend with respect to Pt loading (Figure 3d, e). Importantly, all Pt/TMC catalysts in Figure 3 showed higher ECSA-normalized activity than Pt/C, in particular at low potentials, suggesting a synergistic interaction between Pt and the TMC substrates for glycerol oxidation.

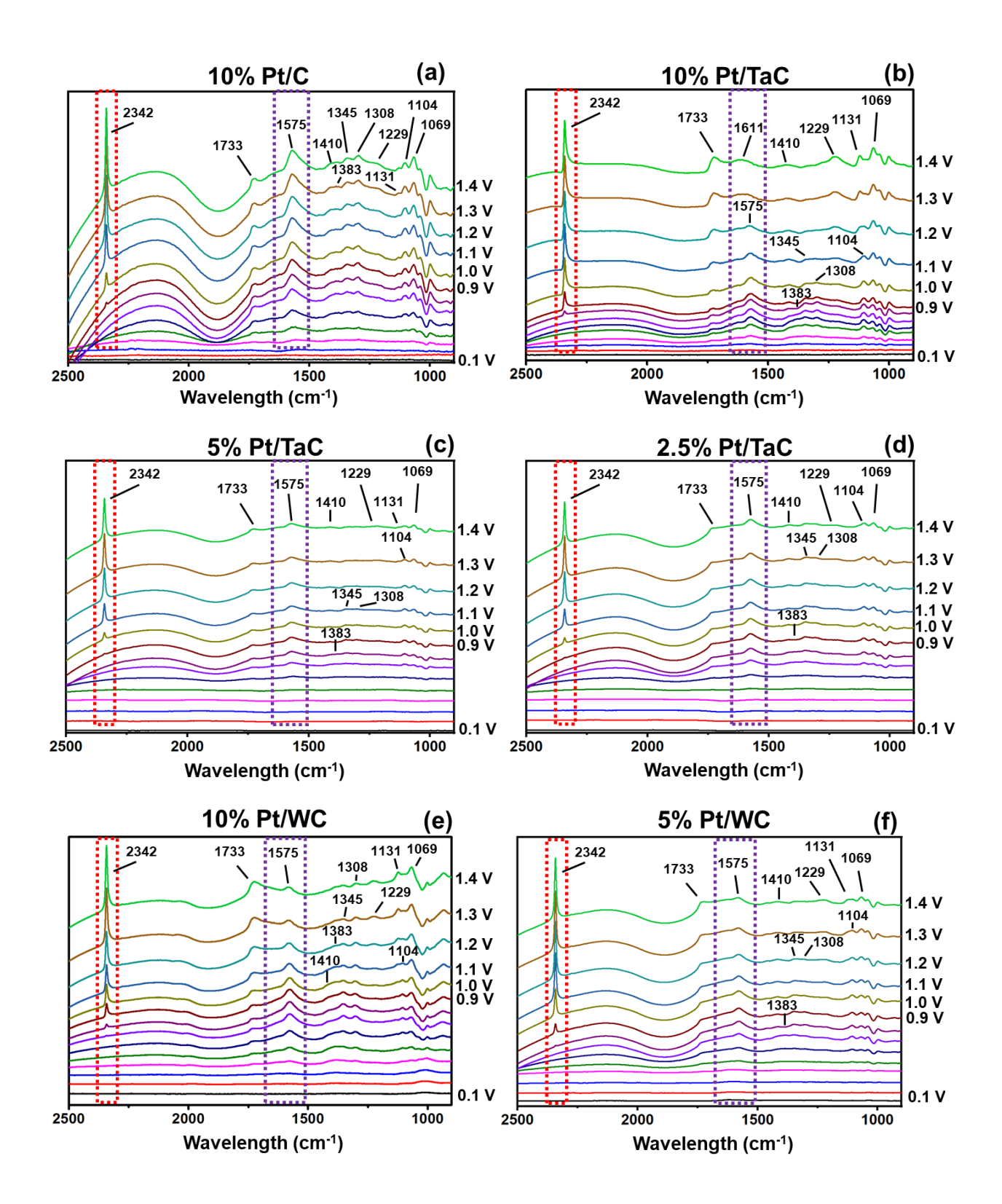
The CA curves revealed that the overall stability followed similar trends among all catalysts studied, with 5 wt% Pt/TaC exhibiting the highest final activity among the catalysts (Figure 3f). This was followed by 2.5 wt% Pt/TaC and 10 wt% Pt/WC. Among all 7 catalysts, only 10 wt% Pt/WC appeared to reach a stabilized state, while the activity of the other catalysts continued to show decay up to the end of the hourlong experiment.

3.3 In-situ FTIR Measurements

FTIR measurements for glycerol oxidation were performed to further understand the advantages of Pt/TMC catalysts over Pt/C. Based on the FTIR results (Figure 4a-g), all catalysts showed a similar variety of oxygenated intermediates above 0.4 V, indicating the partial oxidation of glycerol to various carboxylic acids based on vibrational assignment of FTIR results based on an array of published reference data [43–46]. The 10 wt% Pt/C FTIR plots showed a multitude of alcohol, and carboxylate, and ketone peaks (1069 cm⁻¹, 1104 cm⁻¹, 1131 cm⁻¹, 1229 cm⁻¹, 1308 cm⁻¹, 1326 cm⁻¹, 1345 cm⁻¹, 1383 cm⁻¹, 1410 cm⁻¹, 1575 cm⁻¹, and 1733 cm⁻¹) beginning at 0.5 V, which indicated the presence of glycerate ions, glyceric acid, dihydroxyacetone, glyceraldehyde, glyoxylic acid, tartronic acid, oxalic acid, glycolic acid, formic acid (Figure 4a). This indicated that Pt can cleave C-C bonds on glycerol beginning at low potentials. However, the CO₂ peak (2342 cm⁻¹) appeared starting at 0.9 V vs RHE.

By comparison, 10 wt% Pt/TaC showed the peak at 1383 cm⁻¹ diminishing starting at 0.8 V, which coincided with the appearance of CO₂ (2342 cm⁻¹). The peaks at 1308 cm⁻¹ and 1345 cm⁻¹ diminished after 1.0 V. These changes likely indicated the conversion of oxalic acid and formic acid to CO₂. In addition, the peaks at 1131 cm⁻¹, 1229 cm⁻¹, and 1733 cm⁻¹ also grew starting at 1.2 V. This indicated an accumulation of species including tartronic acid, mesoxalic acid, glyoxylic acid, and glycolic acid, likely as a result of catalyst oxidation at those high potentials. 10 wt% Pt/WC showed a many of the same signals, though

without a significant decrease at 1383 cm⁻¹ (Figure 4e). This suggested that formic acid was not converted to CO₂ as readily as in the case for 10 wt% Pt/TaC, and this is reflected in the higher CO₂ selectivity for 10 wt% Pt/TaC as demonstrated by the peak area ratios between CO₂ (2342 cm⁻¹) and the aggregate carboxylic acids (1575 cm⁻¹) (Figure 4h). Both 10 wt% Pt/TaC and 10 wt% Pt/WC showed earlier onset potentials and greater selectivity for CO₂ when compared against 10 wt% Pt/C.



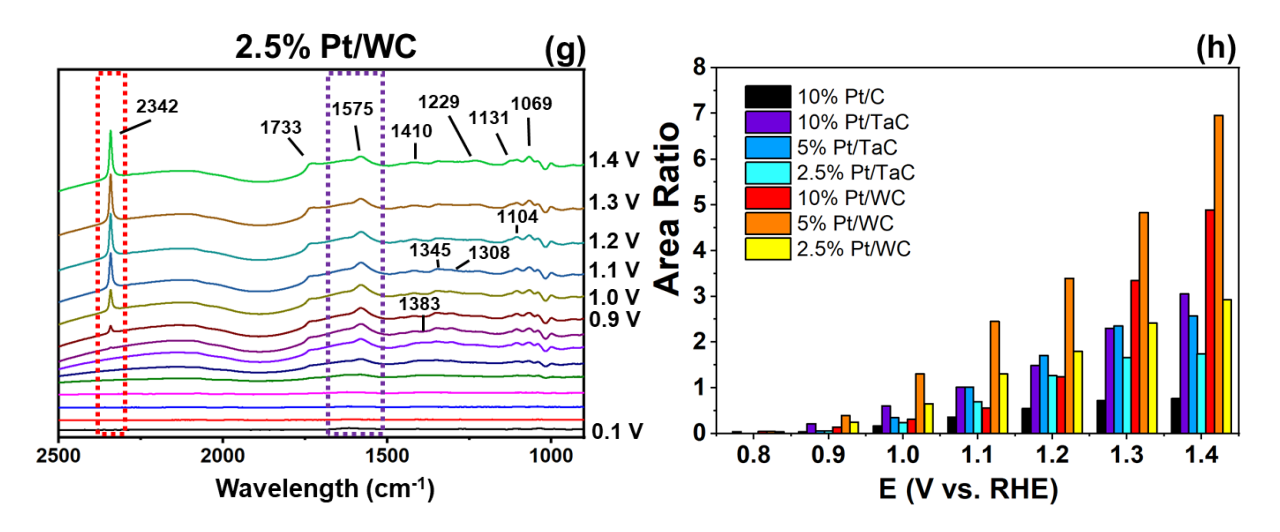


Figure 4. *In-situ* FTIR data of the electrode surface from 0 V to 1.4 V vs RHE for: (a) 10 wt% Pt/C, (b) 10 wt% Pt/TaC, (c) 5 wt% Pt/TaC, (d) 2.5 wt% Pt/TaC, (e) 10 wt% Pt/WC, (f) 5 wt% Pt/WC, and (g) 2.5 wt% Pt/WC, with highlights for the CO₂ peak (red box) and carboxylic acids peak (purple box); (h) area ratio between the carboxylic acid peak and CO₂ peak for each catalyst.

FTIR was used to compare the effect of different Pt mass loadings as well. The results revealed that Pt/TaC samples with lower Pt loading generally showed smaller peaks across the spectrum, with the exception of the general carboxylic acid peak and CO₂ peak (Figure 4b-g). For Pt/WC, 5 wt% Pt/WC and 2.5 wt% Pt/WC both showed a noticeable decrease in peak size at 1308 cm⁻¹ and 1383 cm⁻¹, coinciding with the onset of the CO₂ peak. In conjunction with the greater CO₂ selectivity as compared with 10 wt% Pt/WC, (Figure 4h), this further indicated that these Pt/TMC catalysts enhanced CO₂ selectivity by promoting the oxidation of formic acid and oxalic acid. The persistence of signals from C2 and C3 species, such as glycolic acid, glyoxylic acid, tartronic acid, mesoxalic acid, dihydroxyacetone, and glyceraldehyde (1069 cm⁻¹, 1104 cm⁻¹, 1131 cm⁻¹, 1229 cm⁻¹, 1326 cm⁻¹, 1345 cm⁻¹, 1410 cm⁻¹, 1575 cm⁻¹, and 1733 cm⁻¹) suggested that the oxidation of these molecules to oxalic acid and formic acid remained as the major obstacle in the complete oxidation of glycerol. While Pt/TMC catalysts demonstrated smaller peaks in comparison to 10 wt% Pt/C, the 10 wt% Pt/TaC and 10 wt% Pt/WC catalysts showed stronger signals at

those positions than the lower Pt loading catalysts, suggesting that the increased Pt loading decreased the synergy between the Pt and TMC supports.

The most critical peaks for FTIR analysis were those at 2342 cm⁻¹ and 1575 cm⁻¹. The peak at 1575 cm⁻¹ was an indication of carboxylate ions from a multitude of species, such as glycerate, tartronic acid, mesoxalic acid, glyceric acid, glycolic acid, and glyoxylic acid, and could therefore be referenced as a general carboxylic acid signal [43–46]. Using this carboxylic acid peak as a reference, a comparatively larger CO₂ peak would suggest that the catalyst is more effective at C-C bond scission. By comparing the FTIR peak ratios in Figure 4h, the Pt/TaC and Pt/WC catalysts showed a significant enhancement towards the conversion of glycerol to CO₂ as compared against commercial 10 wt% Pt/C. This result pointed toward a synergistic effect between Pt and the underlying TMC, similar to that described for Pt/TMCs in ethanol oxidation [10,11]. This synergy enhanced the capability of Pt for breaking the C-C bond and completely oxidizing the intermediates.

The 10 wt% Pt/TaC, 10 wt% Pt/WC, 5 wt% Pt/WC, and 2.5 wt% Pt/WC samples showed the earliest onset potential for CO₂ production at 0.8 V, while the 10 wt% Pt/C, 5 wt% Pt/TaC, and 2.5 wt% Pt/TaC samples had onset potentials of 0.9 V. However, the 5 wt% loading for both Pt/TaC and Pt/WC appeared to be optimal. For Pt/TaC, the 5 wt% loading resulted in similar peak area ratios to those of 10 wt% Pt/TaC, while for Pt/WC, the 5 wt% loading showed significantly greater selectivity toward CO₂ than the 10 wt% Pt/WC sample. In contrast, 2.5 wt% Pt/TaC showed less selectivity across all measured potentials, and though the 2.5 wt% Pt/WC showed greater CO₂ selectivity at 0.8 V than 10 wt% Pt/WC, it never exceeded that of 5 wt% Pt/WC and was outclassed by 10 wt% Pt/WC above 1.2 V. From 0.9 V and above, the 2.5 wt% Pt/WC showed similar CO₂ selectivity as 5 wt% and 10 wt% Pt/TaC. Overall, all six Pt/TMC catalysts showed significant improvement to CO₂ selectivity when compared against 10 wt% Pt/C. These results further confirm the synergistic effect from interactions at the Pt-TMC interface for glycerol oxidation.

3.4 In-situ XAFS Characterization

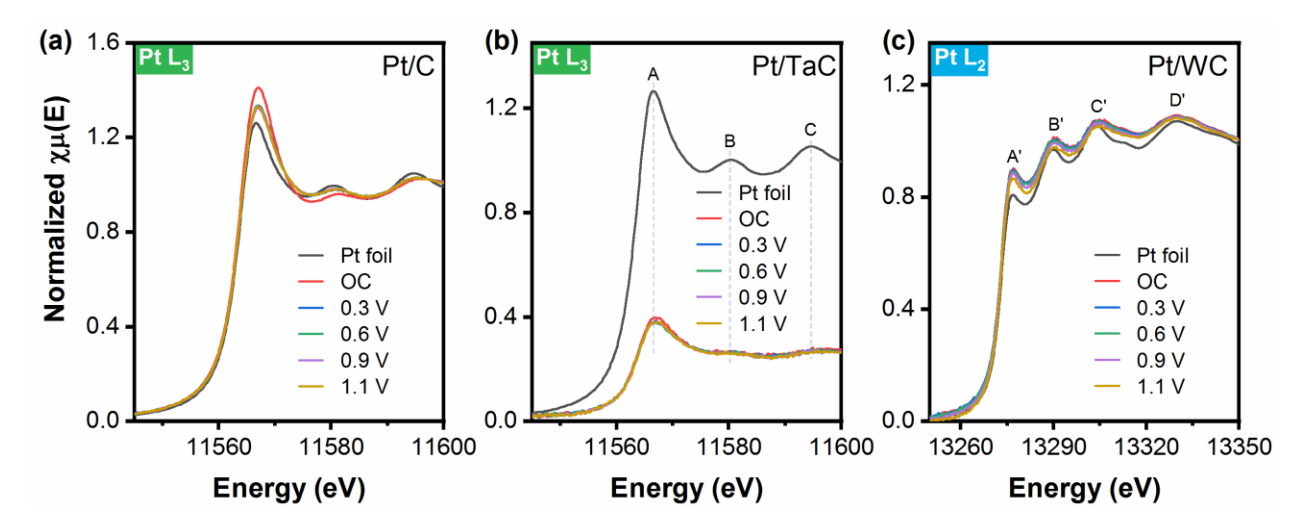


Figure 5. *In-situ* XAFS spectra measured under the glycerol oxidation reaction as the potential increased from OC (0.0 V) to 1.4 V vs RHE. (a) 10 wt% Pt/C, (b) 10 wt% Pt/TaC, and (c) 10 wt% Pt/WC.

To probe the chemical states of Pt under the glycerol oxidation reaction, the *in-situ* XAFS measurements were carried out for the Pt/C (L₃ edge), Pt/TaC (L₃ edge) and Pt/WC (L₂ edge) catalysts at different potentials (0.0, 0.3, 0.6, 0.9, and 1.1 V). As shown in Figure 5a, the Pt/C catalyst exhibited a dominantly metallic feature at the open circuit (OC) condition with a slightly stronger white line than the Pt foil, which became more prominent as the potential exceeded 0.3 V. As for the Pt/TaC catalyst, despite the interference of the Ta L₁ edge, the characteristic resonance peaks (see peaks A-D in Figure 5b) associated with the metallic Pt were clearly observed and the metallic feature retained from OC to 1.1 V. Likewise, a prominent metallic feature (see peaks A'-D' in Figure 5c) was also observed over the Pt/WC catalyst with a gradual reduction as the potential was increased from OC to 1.1 V. Overall, the *in-situ* results revealed that Pt remained in the metallic state for all three catalysts during glycerol oxidation, indicating that the enhanced performance of Pt/TMC over Pt/C was not due to changes in Pt oxidation states. This observation provides input for constructing models of metallic Pt over TMC substrates in DFT calculations, as described next.

3.5 DFT Calculations

DFT calculations were carried out to compute the binding energy (BE) of CO and glycerol on Pt(111), Pt/TaC(111), and Pt/WC(001) surfaces. The DFT optimized geometries in Figure 6 show that CO binds at a hollow site on Pt(111) and Pt/TaC(111), while a top site is a preferred site for CO adsorption on Pt/WC(001). The binding of glycerol occurs via the interaction of OH functional group with surface Pt atoms. Pt/TaC and Pt/WC demonstrated an enhanced glycerol BE compared to Pt (Table 2), which should favor the adsorption and subsequent decomposition of glycerol on the Pt/TMC catalysts. At the same time, compared to Pt(111), the CO BE is reduced on Pt/TaC and Pt/WC (Table 2), consistent with the experimental observation of more facile oxidation of adsorbed CO to CO₂.

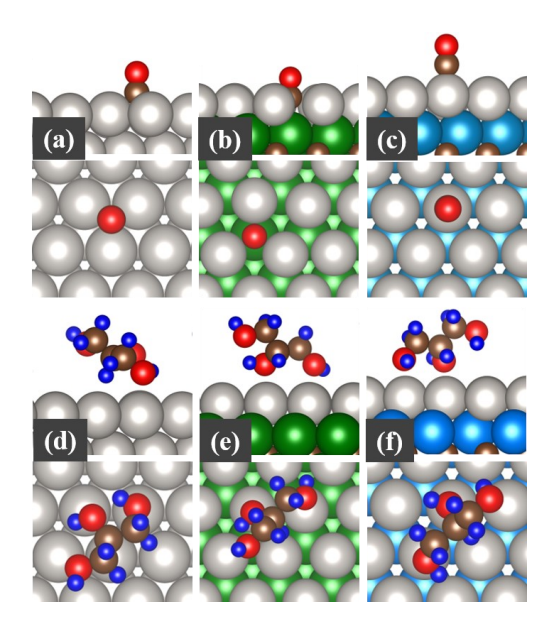


Figure 6. DFT optimized geometries of CO [(a), (b) and (c)], and glycerol [(d), (e) and (f)] on Pt(111), Pt/TaC(111) and Pt/WC(001), respectively. Pt: gray, Ta: green, W: light blue, C: brown, O: red and H: dark blue.

Table 2. Binding energy (BE) of CO and glycerol on Pt(111) and 1 ML Pt supported on WC(001) and TaC(111) as calculated by DFT.

Surface	CO	Glycerol
Pt(111)	-1.76	-0.66

Pt/WC(001)	-1.68	-1.00	
Pt/TaC(111)	-1.35	-0.71	

4 Conclusions

To effectively utilize glycerol as an anodic fuel, it is necessary to optimize catalysts for effective C-C bond cleavage and complete oxidation of reaction intermediates prior to desorption. The current study provided evidence that glycerol oxidation could be enhanced by the interactions of Pt with the TaC and WC substrates. The TMC-supported Pt catalysts showed higher activity for complete glycerol oxidation than commercial 10 wt% Pt/C. Among the Pt/TMC catalysts, 5 wt% Pt/TaC proved to be as active as 10 wt% Pt/TaC and almost as selective for complete glycerol oxidation, while also being more stable. Future studies should further explore the synergistic interactions by supporting Pt over other TMC substrates to further reduce Pt loading while enhancing the complete oxidation of glycerol.

Appendix A. Supplementary Information

Supplementary information related to this article can be found in the associated document.

Acknowledgements

We acknowledge support by the U.S. DOE, Office of Basic Energy Sciences, Catalysis Science Program (Grant No. DE-FG02-13ER16381). Hansen Mou acknowledges support by the National Science Foundation Graduate Research Fellowship under Grant No. DGE 2036197. Shyam Kattel acknowledges the support from the National Science Foundation (Grant No. HRD 2055012). This research used resources of the Center for Functional Nanomaterials (CFN) and beamlines 8-ID (ISS) and 7-BM (QAS) of the National Synchrotron Light Source II (NSLS-II) at Brookhaven National Laboratory (Contract No. DE-SC0012704 and DE-SC0012653) and were supported in part by the Synchrotron Catalysis Consortium (Grant No. DE-SC0012653). The DFT calculations were performed using computational resources at the Extreme Science and Engineering Discovery Environment, which is supported by the National Science Foundation Grant number ACI-1548562.

References

- [1] X. Luo, X. Ge, S. Cui, Y. Li, Value-added processing of crude glycerol into chemicals and polymers, Bioresour. Technol. 215 (2016) 144–154. https://doi.org/10.1016/j.biortech.2016.03.042.
- [2] C.A.G. Quispe, C.J.R. Coronado, J.A. Carvalho Jr., Glycerol: Production, consumption, prices, characterization and new trends in combustion, Renew. Sustain. Energy Rev. 27 (2013) 475–493. https://doi.org/10.1016/j.rser.2013.06.017.
- [3] M. Pagliaro, R. Ciriminna, H. Kimura, M. Rossi, C. Della Pina, From Glycerol to Value-Added Products, Angew. Chem. Int. Ed. 46 (2007) 4434–4440. https://doi.org/10.1002/anie.200604694.
- [4] M. Gupta, N. Kumar, Scope and opportunities of using glycerol as an energy source, Renew. Sustain. Energy Rev. 16 (2012) 4551–4556. https://doi.org/10.1016/j.rser.2012.04.001.
- [5] Z. Gholami, A.Z. Abdullah, K.-T. Lee, Dealing with the surplus of glycerol production from biodiesel industry through catalytic upgrading to polyglycerols and other value-added products, Renew. Sustain. Energy Rev. 39 (2014) 327–341. https://doi.org/10.1016/j.rser.2014.07.092.
- [6] B. Katryniok, H. Kimura, E. Skrzyńska, J.-S. Girardon, P. Fongarland, M. Capron, R. Ducoulombier, N. Mimura, S. Paul, F. Dumeignil, Selective catalytic oxidation of glycerol: perspectives for high value chemicals, Green Chem. 13 (2011) 1960–1979. https://doi.org/10.1039/C1GC15320J.
- [7] N. Benipal, J. Qi, Q. Liu, W. Li, Carbon nanotube supported PdAg nanoparticles for electrocatalytic oxidation of glycerol in anion exchange membrane fuel cells, Appl. Catal. B Environ. 210 (2017) 121–130. https://doi.org/10.1016/j.apcatb.2017.02.082.
- [8] E. Antolini, Glycerol Electro-Oxidation in Alkaline Media and Alkaline Direct Glycerol Fuel Cells, Catalysts. 9 (2019) 980. https://doi.org/10.3390/catal9120980.
- [9] Y. Kwon, S.C.S. Lai, P. Rodriguez, M.T.M. Koper, Electrocatalytic Oxidation of Alcohols on Gold in Alkaline Media: Base or Gold Catalysis?, J. Am. Chem. Soc. 133 (2011) 6914–6917. https://doi.org/10.1021/ja200976j.
- [10] Z. Jiang, Q. Zhang, Z. Liang, J.G. Chen, Pt-modified TaC as an efficient electrocatalyst for ethanol oxidation in acid and alkaline electrolytes, Appl. Catal. B Environ. 234 (2018) 329–336. https://doi.org/10.1016/j.apcatb.2018.04.052.
- [11] T.G. Kelly, A.L. Stottlemyer, X. Yang, J.G. Chen, Theoretical and Experimental Studies of Ethanol Decomposition and Electrooxidation over Pt-Modified Tungsten Carbide, J. Electrochem. Soc. 161 (2014) E3165. https://doi.org/10.1149/2.017408jes.
- [12] E.C. Weigert, A.L. Stottlemyer, M.B. Zellner, J.G. Chen, Tungsten Monocarbide as Potential Replacement of Platinum for Methanol Electrooxidation, J. Phys. Chem. C. 111 (2007) 14617–14620. https://doi.org/10.1021/jp075504z.
- [13] S.M. Alia, G. Zhang, D. Kisailus, D. Li, S. Gu, K. Jensen, Y. Yan, Porous Platinum Nanotubes for Oxygen Reduction and Methanol Oxidation Reactions, Adv. Funct. Mater. 20 (2010) 3742–3746. https://doi.org/10.1002/adfm.201001035.
- [14] F. Colmati, G. Tremiliosi-Filho, E. R. Gonzalez, A. Berná, E. Herrero, J. M. Feliu, The role of the steps in the cleavage of the C–C bond during ethanol oxidation on platinum electrodes, Phys. Chem. Phys. 11 (2009) 9114–9123. https://doi.org/10.1039/B907250K.
- [15] W. Zhou, Z. Zhou, S. Song, W. Li, G. Sun, P. Tsiakaras, Q. Xin, Pt based anode catalysts for direct ethanol fuel cells, Appl. Catal. B Environ. 46 (2003) 273–285. https://doi.org/10.1016/S0926-3373(03)00218-2.
- [16] S. Rousseau, C. Coutanceau, C. Lamy, J.-M. Léger, Direct ethanol fuel cell (DEFC): Electrical performances and reaction products distribution under operating conditions with different platinum-based anodes, J. Power Sources. 158 (2006) 18–24. https://doi.org/10.1016/j.jpowsour.2005.08.027.
- [17] Q. Chang, S. Kattel, X. Li, Z. Liang, B.M. Tackett, S.R. Denny, P. Zhang, D. Su, J.G. Chen, Z. Chen, Enhancing C–C Bond Scission for Efficient Ethanol Oxidation using PtIr Nanocube Electrocatalysts, ACS Catal. 9 (2019) 7618–7625. https://doi.org/10.1021/acscatal.9b02039.
- [18] Q. Chang, Y. Hong, H.J. Lee, J.H. Lee, D. Ologunagba, Z. Liang, J. Kim, M.J. Kim, J.W. Hong, L. Song, S. Kattel, Z. Chen, J.G. Chen, S.-I. Choi, Achieving complete electrooxidation of ethanol by

- single atomic Rh decoration of Pt nanocubes, Proc. Natl. Acad. Sci. 119 (2022) e2112109119. https://doi.org/10.1073/pnas.2112109119.
- [19] A. Garg, D.S. Gonçalves, Y. Liu, Z. Wang, L. Wang, J.S. Yoo, A. Kolpak, R.M. Rioux, D. Zanchet, Y. Román-Leshkov, Impact of Transition Metal Carbide and Nitride Supports on the Electronic Structure of Thin Platinum Overlayers, ACS Catal. 9 (2019) 7090–7098. https://doi.org/10.1021/acscatal.9b01272.
- [20] R.B. Levy, M. Boudart, Platinum-Like Behavior of Tungsten Carbide in Surface Catalysis, Science. 181 (1973) 547–549. https://doi.org/10.1126/science.181.4099.547.
- [21] Y. Liu, T.G. Kelly, J.G. Chen, W.E. Mustain, Metal Carbides as Alternative Electrocatalyst Supports, ACS Catal. 3 (2013) 1184–1194. https://doi.org/10.1021/cs4001249.
- [22] M.K. Sahoo, G.R. Rao, Enhanced Methanol Electro-Oxidation Activity of Pt/rGO Electrocatalyst Promoted by NbC/Mo2C Phases, ChemistrySelect. 5 (2020) 3805–3814. https://doi.org/10.1002/slct.202000170.
- [23] H.H. Hwu, J.G. Chen, Surface Chemistry of Transition Metal Carbides, Chem. Rev. 105 (2005) 185–212. https://doi.org/10.1021/cr0204606.
- [24] T.E. Shubina, M.T.M. Koper, Quantum-chemical calculations of CO and OH interacting with bimetallic surfaces, Electrochimica Acta. 47 (2002) 3621–3628. https://doi.org/10.1016/S0013-4686(02)00332-8.
- [25] J. Wang, S. Kattel, C.J. Hawxhurst, J.H. Lee, B.M. Tackett, K. Chang, N. Rui, C.-J. Liu, J.G. Chen, Enhancing Activity and Reducing Cost for Electrochemical Reduction of CO₂ by Supporting Palladium on Metal Carbides, Angew. Chem. Int. Ed. 58 (2019) 6271–6275. https://doi.org/10.1002/anie.201900781.
- [26] L. Wang, E. G. Mahoney, S. Zhao, B. Yang, J. G. Chen, Low loadings of platinum on transition metal carbides for hydrogen oxidation and evolution reactions in alkaline electrolytes, Chem. Commun. 52 (2016) 3697–3700. https://doi.org/10.1039/C5CC10439D.
- [27] J.H. Lee, S. Kattel, Z. Jiang, Z. Xie, S. Yao, B.M. Tackett, W. Xu, N.S. Marinkovic, J.G. Chen, Tuning the activity and selectivity of electroreduction of CO 2 to synthesis gas using bimetallic catalysts, Nat. Commun. 10 (2019) 3724. https://doi.org/10.1038/s41467-019-11352-0.
- [28] B. Ravel, M. Newville, ATHENA, ARTEMIS, HEPHAESTUS: data analysis for X-ray absorption spectroscopy using IFEFFIT, J. Synchrotron Radiat. 12 (2005) 537–541. https://doi.org/10.1107/S0909049505012719.
- [29] B. Ravel, M. Newville, ATHENA and ARTEMIS: interactive graphical data analysis using IFEFFIT, Phys. Scr. 2005 (2005) 1007. https://doi.org/10.1238/Physica.Topical.115a01007.
- [30] G. Kresse, J. Furthmüller, Efficiency of ab-initio total energy calculations for metals and semiconductors using a plane-wave basis set, Comput. Mater. Sci. 6 (1996) 15–50. https://doi.org/10.1016/0927-0256(96)00008-0.
- [31] G. Kresse, J. Hafner, Ab initio molecular dynamics for open-shell transition metals, Phys. Rev. B. 48 (1993) 13115–13118. https://doi.org/10.1103/PhysRevB.48.13115.
- [32] P. Hohenberg, W. Kohn, Inhomogeneous Electron Gas, Phys. Rev. 136 (1964) B864–B871. https://doi.org/10.1103/PhysRev.136.B864.
- [33] W. Kohn, L.J. Sham, Self-Consistent Equations Including Exchange and Correlation Effects, Phys. Rev. 140 (1965) A1133–A1138. https://doi.org/10.1103/PhysRev.140.A1133.
- [34] P.E. Blöchl, Projector augmented-wave method, Phys. Rev. B. 50 (1994) 17953–17979. https://doi.org/10.1103/PhysRevB.50.17953.
- [35] J.P. Perdew, K. Burke, M. Ernzerhof, Generalized Gradient Approximation Made Simple, Phys. Rev. Lett. 77 (1996) 3865–3868. https://doi.org/10.1103/PhysRevLett.77.3865.
- [36] J.P. Perdew, Y. Wang, Accurate and simple analytic representation of the electron-gas correlation energy, Phys. Rev. B. 45 (1992) 13244–13249. https://doi.org/10.1103/PhysRevB.45.13244.
- [37] Y.C. Kimmel, X. Xu, W. Yu, X. Yang, J.G. Chen, Trends in Electrochemical Stability of Transition Metal Carbides and Their Potential Use As Supports for Low-Cost Electrocatalysts, ACS Catal. 4 (2014) 1558–1562. https://doi.org/10.1021/cs500182h.

- [38] K.M. Andersson, L. Bergström, Oxidation and dissolution of tungsten carbide powder in water, Int. J. Refract. Met. Hard Mater. 18 (2000) 121–129. https://doi.org/10.1016/S0263-4368(00)00010-X.
- [39] M. Li, K. Duanmu, C. Wan, T. Cheng, L. Zhang, S. Dai, W. Chen, Z. Zhao, P. Li, H. Fei, Y. Zhu, R. Yu, J. Luo, K. Zang, Z. Lin, M. Ding, J. Huang, H. Sun, J. Guo, X. Pan, W.A. Goddard, P. Sautet, Y. Huang, X. Duan, Single-atom tailoring of platinum nanocatalysts for high-performance multifunctional electrocatalysis, Nat. Catal. 2 (2019) 495–503. https://doi.org/10.1038/s41929-019-0279-6.
- [40] J.-N. Zheng, S.-S. Li, X. Ma, F.-Y. Chen, A.-J. Wang, J.-R. Chen, J.-J. Feng, Popcorn-like PtAu nanoparticles supported on reduced graphene oxide: Facile synthesis and catalytic applications, J. Mater. Chem. A. 2 (2014) 8386–8395. https://doi.org/10.1039/C4TA00857J.
- [41] Q. Chen, B. Wei, Y. Wei, P. Zhai, W. Liu, X. Gu, Z. Yang, J. Zuo, R. Zhang, Y. Gong, Synergistic effect in ultrafine PtNiP nanowires for highly efficient electrochemical hydrogen evolution in alkaline electrolyte, Appl. Catal. B Environ. 301 (2022) 120754. https://doi.org/10.1016/j.apcatb.2021.120754.
- [42] S.-S. Li, J.-J. Lv, L.-N. Teng, A.-J. Wang, J.-R. Chen, J.-J. Feng, Facile Synthesis of PdPt@Pt Nanorings Supported on Reduced Graphene Oxide with Enhanced Electrocatalytic Properties, ACS Appl. Mater. Interfaces. 6 (2014) 10549–10555. https://doi.org/10.1021/am502148z.
- [43] J.F. Gomes, G. Tremiliosi-Filho, Spectroscopic Studies of the Glycerol Electro-Oxidation on Polycrystalline Au and Pt Surfaces in Acidic and Alkaline Media, Electrocatalysis. 2 (2011) 96–105. https://doi.org/10.1007/s12678-011-0039-0.
- [44] M. Simões, S. Baranton, C. Coutanceau, Electro-oxidation of glycerol at Pd based nano-catalysts for an application in alkaline fuel cells for chemicals and energy cogeneration, Appl. Catal. B Environ. 93 (2010) 354–362. https://doi.org/10.1016/j.apcatb.2009.10.008.
- [45] Y. Holade, C. Morais, K. Servat, T.W. Napporn, K.B. Kokoh, Toward the Electrochemical Valorization of Glycerol: Fourier Transform Infrared Spectroscopic and Chromatographic Studies, ACS Catal. 3 (2013) 2403–2411. https://doi.org/10.1021/cs400559d.
- [46] J.F. Gomes, A.C. Garcia, L.H.S. Gasparotto, N.E. de Souza, E.B. Ferreira, C. Pires, G. Tremiliosi-Filho, Influence of silver on the glycerol electro-oxidation over AuAg/C catalysts in alkaline medium: a cyclic voltammetry and in situ FTIR spectroscopy study, Electrochimica Acta. 144 (2014) 361–368. https://doi.org/10.1016/j.electacta.2014.08.035.